Performance and Optimization of the Hydropneumatic Suspension of High-Speed Wheeled Excavators

Zhanlong Li, Shixun Zhao, Bao Sun, Shantie Gao, Yu Gao, Beijun Guo, Zhiqi Liu, and Fuxi Liu

Abstract—**The hydropneumatic suspension has advantages in terms of variable stiffness, compact structure, and carrying capacity. These advantages satisfy the requirements of high-speed wheeled excavators. The present study aimed to investigate the performance of the hydropneumatic suspension of high-speed wheeled excavators. The performances of the hydropneumatic suspension and leaf spring were compared. The hydropneumatic suspension was found to perform better compared with the leaf spring suspension. The multiobjective optimization was employed to optimize the hydropneumatic suspension parameters. The results showed that the vertical acceleration, suspension working space, and dynamic tire load decreased by 22.4%, 23.0%, and 0.62%, respectively.**

Index Terms—**Artificial physics optimization algorithm, high-speed wheeled excavators, hydropneumatic suspension, leaf spring suspension**

I. Introduction

Wheeled excavators have been widely used in urban municipal construction fields, such as pipeline laying, green construction, and housing demolition. The wheeled excavators for civilian use have a speed of about 40 km/h, while the wheeled excavators produced by the JCB company can reach a speed of 100 km/h. The promotion of the speed of wheeled excavators may lead to a deterioration of the vibration condition of wheeled excavators. A suspension, including leaf spring suspension, air spring suspension, and hydropneumatic suspension, was introduced into wheeled excavators to solve this problem. The leaf spring suspension had good reliability and variable stiffness, but poor adaptability to the uneven road surface. The air spring suspension had good comfort and variable stiffness, but was easily damaged by the impact of foreign bodies. The hydropneumatic suspension had a nonlinear spring characteristic [1]. Therefore, the hydropneumatic suspension is generally used in mining dump trucks, all-terrain cranes, military vehicles, and special vehicles [2].

In recent years, many researchers have started paying attention to the hydropneumatic suspension. In a previous study [3], a mathematical model of the hydropneumatic suspension for military tracked vehicles was constructed. The life of a hydropneumatic suspension could be enhanced by optimizing the load transferring leverage ratio [4]. A previous study [5] investigated the influence of hydropneumatic parameters on the ride safety of tracked vehicles. Another study [6] investigated the influence of the hydropneumatic suspension on the dynamic characteristics of tractors. The various layouts of the hydropneumatic suspension were investigated to alleviate the harsh vibration of the wheel loaders [7]–[8]. However, the performance and optimization of the hydropneumatic suspension of high-speed wheeled excavators were rarely investigated.

This study investigated the performance and optimization of the hydropneumatic suspension of high-speed wheeled excavators. First, the mathematical model of the hydropneumatic suspension of high-speed wheeled excavators was established. Second, the performances of the hydropneumatic suspension and leaf spring were compared. Finally, the hydropneumatic suspension parameters were optimized.

II. Mathematical Model

Fig. 1 shows the schematic diagram of a hydropneumatic suspension of high-speed wheeled excavators. The hydropneumatic suspension consists of a cylinder, a rod, and a piston. The hydropneumatic suspension provides a variable sealed chamber. The suspension motion alters the volume of the gas and fluid in each chamber and exhibits different spring and damping characteristics. The hydropneumatic suspension generates the damping force with the

Manuscript received September 13, 2022; revised April 2, 2023. This study was supported by the National Natural Science Foundation of China (Grant No. 52272401), the Fundamental Research Program of Shanxi Province (Grant No. 202203021211185), the Excellent Innovation Project for Graduate Students in Shanxi Province (Grant No. 2022Y679), and the Xinzhou City Science and Technology Plan Project - Key Research and Development Plan (Grant No. 20220107).

Zhanlong Li is an associate professor at the School of Mechanical Engineering, Taiyuan University of Science and Technology, Taiyuan 030024, China (e-mail: lizl@tyust.edu.cn).

Shixun Zhao is a postgraduate from the School of Mechanical Engineering, Taiyuan University of Science and Technology, Taiyuan 030024, China (e-mail: 529273009@qq.com).

Bao Sun is an associate professor at the School of Applied Science, Taiyuan University of Science and Technology, Taiyuan 030024, China (e-mail: Bao810321@163.com).

Shantie Gao is an engineer at the Guizhou Jonyang Kinetics Co., Ltd., Guiyang 550006, China (e-mail: gaoshantie@jonyang.com).

Yu Gao is a postgraduate from the School of Mechanical Engineering, Taiyuan University of Science and Technology, Taiyuan 030024, China (e-mail: 895352518@qq.com).

Beijun Guo is an engineer at the Shanxi Jiacheng Hydraulic Co., Ltd., Xinzhou 034100, China (e-mail: jc_gbj@163.com).

Zhiqi Liu is a professor at the School of Mechanical Engineering, Taiyuan University of Science and Technology, Taiyuan 030024, China (e-mail: liuzhiqi@tyust.edu.cn).

Fuxi Liu is a teacher at the School of Mechanical and Electrical Engineering, Hunan Applied Technology University, Changde 415100, China. Correspondence should be addressed to Fuxi Liu, e-mail: liufx28@163.com.

compression and rebound of the cylinder [9]–[11].

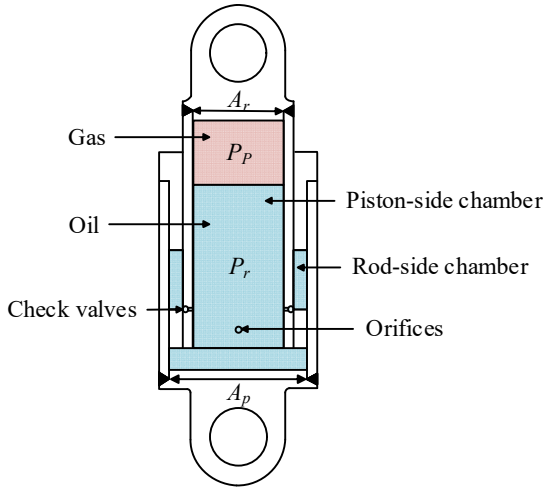

Fig. 1. Schematic diagram of the hydro-pneumatic suspension of high-speed wheeled excavators

The total force acting on the piston rod F can be expressed as follows:

$$F = P_p \cdot A_p - P_r(A_p - A_r) + f \tag{1}$$

where P_p is the pressure of the piston-side chamber, P_r is the pressure of the rod-side chamber, A_p is the effective cross-sectional area of the piston-side chamber, A_r is the effective cross-sectional area of the rod-side chamber, and f is the friction force generated by the sealing element.

The state equation is expressed as:

$$P_p \cdot V_g^{\alpha} = P_0 \cdot V_{g0}^{\alpha} \tag{2}$$

where V_g is the gas instantaneous volume, P_0 is the initial gas pressure, V_{g0} is the initial gas volume, and α is the polytropic exponent.

The gas volume V_g is expressed as:

$$V_g = V_{g0} - A_r \cdot x \tag{3}$$

where x is the compression displacement of the suspension cylinder.

The spring force F_k is expressed as:

$$F_k = P_0 \cdot \left(\frac{V_{g0}}{V_{g0} - A_r \quad x}\right)^{\alpha} \cdot A_r \tag{4}$$

According to the small-hole flow equation, the oil flow through the orifices and check valve is expressed as:

$$Q = C_q \cdot A \cdot \sqrt{\frac{2\Delta P}{\rho}} = (A_p - A_r)\dot{x} \tag{5}$$

where C_q is the discharge coefficient, A is the fluid flow area, ΔP is the pressure difference between the rod-side chamber and the piston-side chamber, ρ is the average density of the piston and rod-side chamber, and $\dot{x}$ is the compression speed.

The damping force F_v is expressed as:

$$F_v = \frac{\rho}{2} \cdot \frac{\dot{x}^2 \cdot (A_p - A_r)^3 \cdot sign(\dot{x})}{C_q^2 \left(m \cdot A_k + n \cdot A_f (0.5 + 0.5 sign(\dot{x}))\right)} \tag{6}$$

where A_k is the opening area of the orifices, m is the number of orifices, A_f is the opening area of the check valves, and n is the number of check valves.

The total force F is expressed as:

$$F = F_k + F_v \tag{7}$$

III. Parameter Study

A parametric study was conducted based on the established mathematical model. The parameters of the hydropneumatic cylinder for a high-speed wheeled excavator are listed in Table 1.

TABLE 1
Parameters of the Hydropneumatic Cylinder for a High-Speed Wheeled Excavator

Symbol	Name	Value
P_0	Initial gas pressure	5.76 MPa
V_{g0}	Initial gas volume	0.50 L
A_r	Cross-sectional area of the rod	5200.00 mm^2
A_p	Cross-sectional area of the piston	7900.00 mm^2
A_k	Opening area of the orifices	7.00 mm^2
A_f	Opening area of the check valves	28.00 mm^2
ρ	Hydraulic oil density	900.00 kg/m^3
β	Hydraulic oil bulk modulus	1300.00 MPa
n	Polytropic exponent	1.40
C_q	Discharge coefficient	0.62

Fig. 2 shows the effects of the initial gas pressure, initial gas volume, cross-sectional area of the rod, cross-sectional area of the piston, opening area of the orifices, and opening area of the check valves on the spring force. The figure shows that the spring force was controlled by the initial gas pressure, initial gas volume, and cross-sectional area of the piston. The reason for this phenomenon was that the initial gas pressure, initial gas volume, and cross-sectional area of the piston could cause the compression and expansion of the high-pressure gas. Further, as shown in Fig. 2, the spring force increased with the increase in the displacement.

Fig. 3 presents the effects of the initial gas pressure, initial gas volume, cross-sectional area of the rod, cross-sectional area of the piston, opening area of the orifices, and opening area of the check valves on the damping force. It is observed from Fig. 3 that the damping force was controlled by the cross-sectional area of the rod, cross-sectional area of the piston, opening area of orifices, and opening area of check valves. The reason for this phenomenon was that the cross-sectional area of the rod, cross-sectional area of the piston, opening area of orifices, and opening area of check valves could cause the flow of fluid through the orifice and check valves.

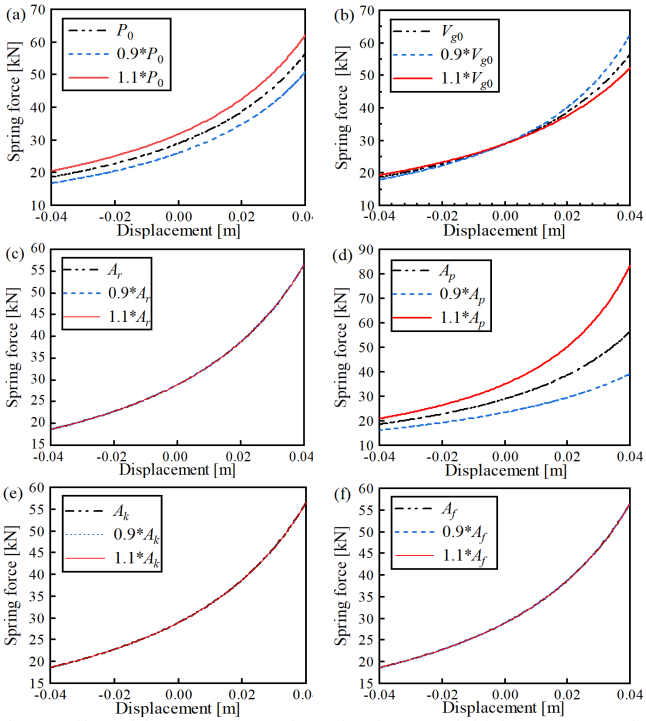

Fig. 2. Effect of the parameter on the spring force: (a) initial gas pressure, (b) initial gas volume, (c) cross-sectional area of the rod, (d) cross-sectional area of the piston, (e) opening area of the orifices, and (f) opening area of the check valves.

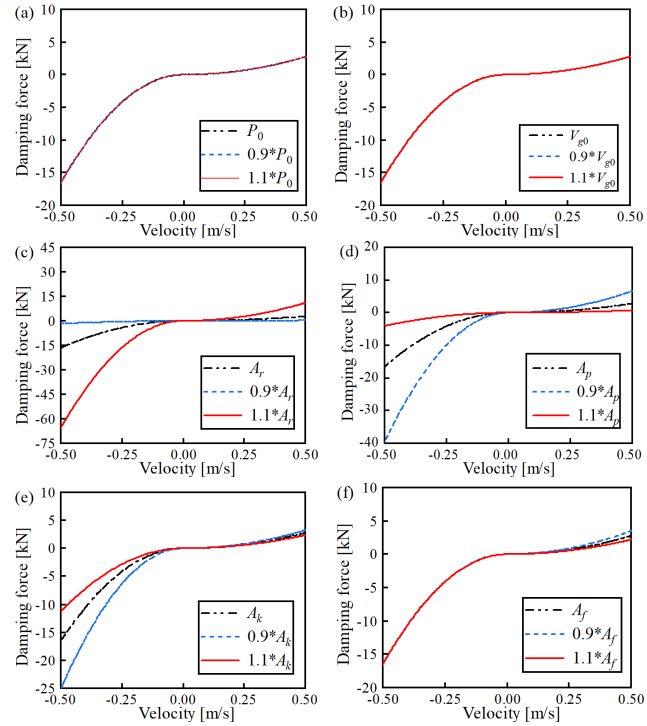

Fig. 3. Effect of the parameter on the damping force: (a) initial gas pressure, (b) initial gas volume, (c) cross-sectional area of the rod, (d) cross-sectional area of the piston, (e) opening area of the orifices, and (f) opening area of the check valves.

IV. Performance of the Suspension System

The model of the hydropneumatic suspension and leaf spring suspension was established using the Amesim software, as shown in Fig. 4.

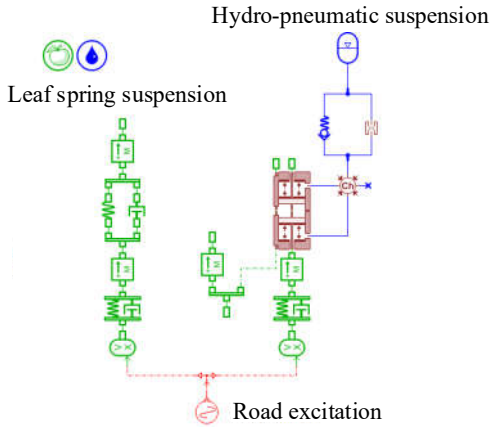

Fig. 4. Model of the hydropneumatic suspension and leaf spring suspension.

A. Uneven roads

When the high-speed wheeled excavators drive on uneven roads, a pulse shock is produced [12]–[15]. $x(t)$ is the displacement of the pulse disturbance and expressed as follows:

$$x(t)=\frac{A}{2}(1-\cos(2\pi(\frac{v}{l})t)),\quad 0\le t\le\frac{l}{v} \tag{8}$$

where v is the speed of high-speed wheeled excavators, A is the slope height, and l is the slope width.

Fig. 5 shows the pulse shock-response curves of the hydropneumatic suspension and leaf spring suspension. The vibration amplitude of the hydropneumatic suspension was found to be obviously less than that of the leaf spring suspension. This result indicated that the hydropneumatic suspension performed better than the leaf spring suspension on uneven roads.

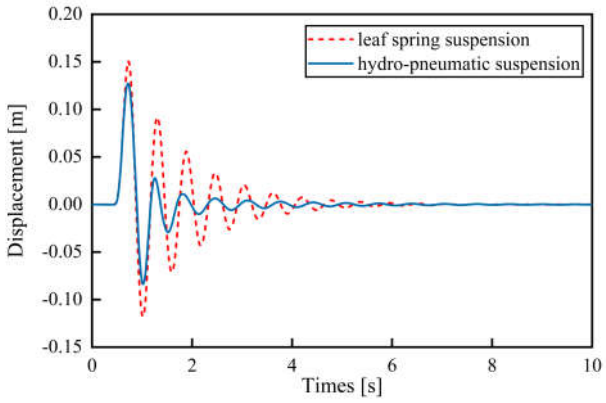

Fig. 5. Pulse shock-response curves of the hydropneumatic suspension and leaf spring suspension (v = 25 km/h, A = 180 mm, and l = 5000 mm).

Fig. 6 shows the experiments of high-speed wheeled excavators driving on uneven roads. In Fig. 6, the speed of the high-speed wheeled excavator was 20 km/h, and the acceleration sensors were installed at the excavator frame in the vertical direction. The vertical acceleration was obtained using the acceleration sensors. According to the obtained vertical acceleration, the root-mean-square (RMS) value of the vertical acceleration of the hydropneumatic suspension was 1.37 m/s^2 while that of the leaf spring suspension was 1.83 m/s^2. This result indicated that the hydropneumatic

suspension performed better compared with the leaf spring suspension on uneven roads. The experimental result proved that the simulation result was correct.

Fig. 6. Experiments of high-speed wheeled excavators driving on uneven roads.

B. *Flat roads*

When the high-speed wheeled excavators drive on flat roads, a random vibration is produced [16]–[17]. $\dot{x}(t)$ is the speed of the disturbance and is described as follows:

$$\dot{x}(t) = -2\pi f_0 x(t) + 2\pi n_0 w(t)\sqrt{G_q(n_0)v} \tag{9}$$

where f_0 is the lower limiting frequency of the wave filter, n_0 is the suggested spatial frequency, $G_q(n_0)$ is the coefficient of the pavement irregularity, and $w(t)$ is the frequency index.

The suspension system could supply sufficient ride comfort and anti-rollover stability. The evaluation index of the suspension system included the vertical acceleration, suspension working space, and dynamic tire load [18].

Figs. 7-9 show the response curves of the hydropneumatic suspension and leaf spring suspension. The figures show that the hydropneumatic suspension performed better compared with the leaf spring suspension on flat roads.

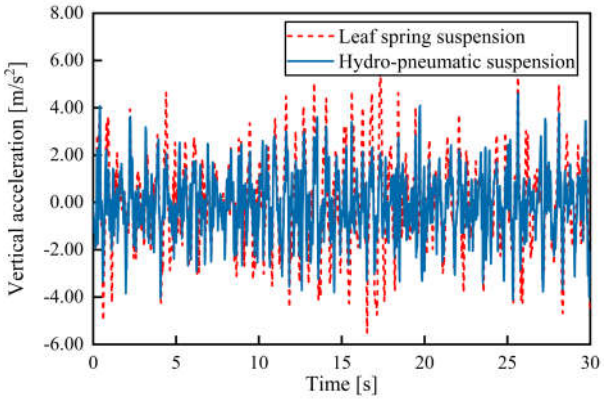

Fig. 7. Comparison of the vertical accelerations of the hydropneumatic and leaf spring suspensions (v = 55 km/h).

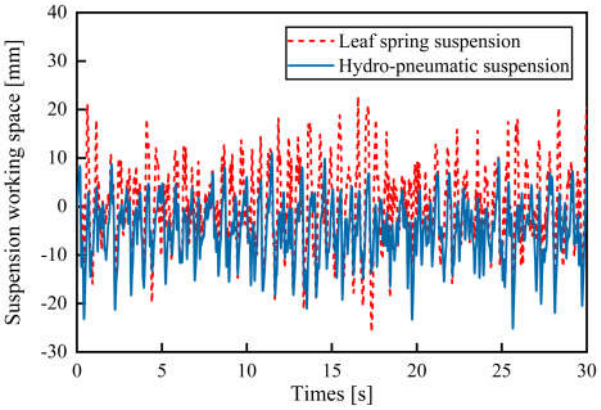

Fig. 8. Comparison of the suspension working spaces of the hydropneumatic and leaf spring suspensions (v = 55 km/h).

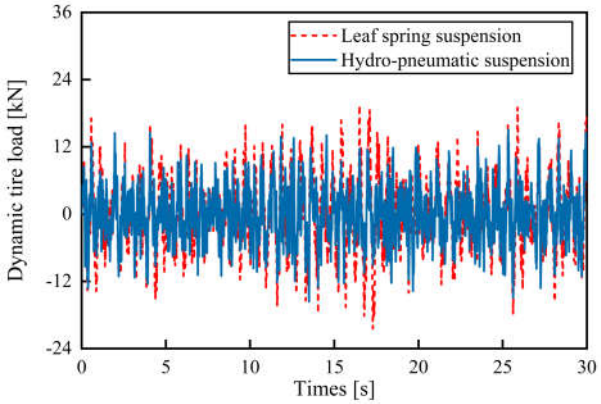

Fig. 9. Comparison of the dynamic tire loads of the hydropneumatic and leaf spring suspensions (v = 55 km/h).

Fig. 10 shows the experiments of high-speed wheeled excavators driving on flat roads. The speed of the high-speed wheeled excavator was 60 km/h. The vertical acceleration was obtained using the acceleration sensors. The RMS value of the vertical acceleration of the hydropneumatic suspension was 0.43 m/s^2 while that of the leaf spring suspension was 0.51 m/s^2. This result indicated that the hydropneumatic suspension performed better compared with the leaf spring suspension on flat roads. The experimental result also proved that the simulation result was correct.

Fig. 10. Experiments of high-speed wheeled excavators driving on uneven roads.

V. MULTIOBJECTIVE OPTIMIZATION OF HYDROPNEUMATIC SUSPENSION PARAMETERS

A. Establishment of multiobjective optimization model

The multiobjective optimization model is expressed as:

$$\begin{cases} \min \quad f_1(P_0, V_{g0}, d_k, d_f) = \text{VA} \\ \min \quad f_2(P_0, V_{g0}, d_k, d_f) = \text{SWS} \\ \min \quad f_3(P_0, V_{g0}, d_k, d_f) = \text{DTL} \\ s.t. \quad \sigma_n = \frac{1}{3}[f_d] \\ \qquad \sigma_f = \frac{1}{3}G \end{cases} \tag{10}$$

$$5.18 \le P_0 \le 6.34$$
$$0.45 \le V_{g0} \le 0.55$$
$$2 \le d_k \le 5$$
$$4 \le d_f \le 8$$

where VA is the vertical acceleration, SWS is the suspension working space, DTL is the dynamic tire load, σ_n is the suspension working space RMS value, $[f_d]$ is the limit stroke value, σ_f is the dynamic tire load RMS value, G is the static tire load, d_k is the diameter of the orifice, and d_f is the diameter of the check valve.

B. Multiobjective optimization

In this study, the multiobjective optimization was based on the artificial physics optimization algorithm (APOA). The APOA is a novel stochastic optimization algorithm with high calculating speed and good population diversity [19]–[21]. The optimization process of the APOA is shown in Fig. 11.

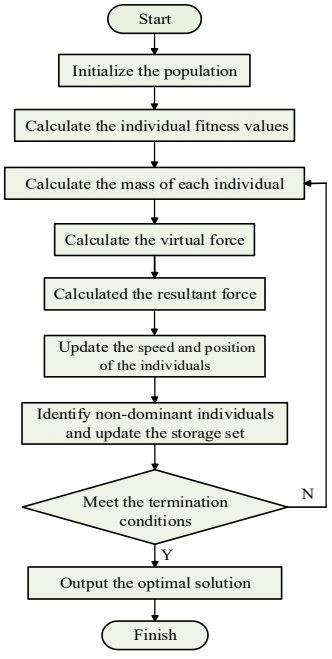

Fig. 11. Optimization process of the APOA.

The steps of the APOA are as follows [22]:

Step 1: The multiobjective optimization starts.

Step 2: The population is initialized.

Step 3: The individual fitness values are calculated.

Step 4: The mass of each individual is calculated. The mass of the *i*th individual m_i is expressed as:

$$m_i = e^{\frac{f(x_{best}) - f(x_i)}{f(x_{worst}) - f(x_{best})}} \tag{11}$$

where $f(x_{best})$ is the function value of the best individual x_{best}, $f(x_{worst})$ is the function value of the worst individual x_{worst}, and $f(x_i)$ is the function value of the *i*th individual x_i.

Step 5: The virtual force of the *j*th individual on the *k*th dimension is calculated. The calculated virtual force $F_{ij,k}$ is expressed as:

$$F_{ij,k} = \begin{cases} Gm_i m_j (x_{j,k} - x_{i,k}), & f(x_i) > f(x_j) \\ -Gm_i m_j (x_{j,k} - x_{i,k}), & f(x_i) \le f(x_j) \end{cases} \tag{12}$$

where G is the gravitational constant, $x_{i,k}$ is the position of the *i*th individual on the *k*th dimension, and $x_{j,k}$ is the position of the *j*th individual on the *k*th dimension.

Step 6: The resultant force is calculated. The calculated resultant force $F_{i,k}$ is expressed as:

$$F_{i,k} = \sum_{j=1}^{n} F_{ij,k} \tag{13}$$

where n is the population size.

Step 7: The speed and position of the individuals are updated. The updated speed $v_{i,k}(t+1)$ is expressed as:

$$v_{i,k}(t+1) = wv_{i,k}(t) + \lambda F_{i,k} / m_i \tag{14}$$

where w is the inertia weight, λ is the random variable, and $v_{i,k}(t)$ is the original speed.

The updated position $x_{i,k}(t+1)$ is expressed as:

$$x_{i,k}(t+1) = x_{i,k}(t) + v_{i,k}(t+1) \tag{15}$$

where $x_{i,k}(t)$ is the original position.

Step 8: The nondominant individuals are identified, and the archive set is updated.

Step 9: If the termination conditions are met, the optimal solution is output. If the termination conditions are not met, the program goes to Step 4.

Step 10: The program is finished.

C. Multiobjective optimization

Based on the aforementioned steps, the speed of the high-speed wheeled excavators driving on flat roads was 55 km/h, and each simulation time was 20 s. The optimal parameters of the hydropneumatic suspension were obtained using the multiobjective APOA. The hydropneumatic

suspension parameters before and after optimization are shown in Table 2.

TABLE 2
HYDROPNEUMATIC SUSPENSION PARAMETERS BEFORE AND AFTER OPTIMIZATION

Symbol	Name	Before	After
P_0	Initial gas pressure	5.76 MPa	5.49 MPa
V_{g0}	Initial gas volume	0.50 L	0.54 L
d_k	Diameter of the orifice	3.00 mm	2.63 mm
d_f	Diameter of the check valve	6.00 mm	5.86 mm

Fig. 12 shows the comparison of the vertical acceleration RMS value of the hydropneumatic suspension before and after optimization. The vertical acceleration RMS value of the hydropneumatic suspension before optimization was 1.351 m/s^2. The vertical acceleration RMS value of the hydropneumatic suspension after optimization was 1.049 m/s^2. Therefore, the vertical acceleration RMS value of the hydropneumatic suspension decreased by 22.4% using the APOA.

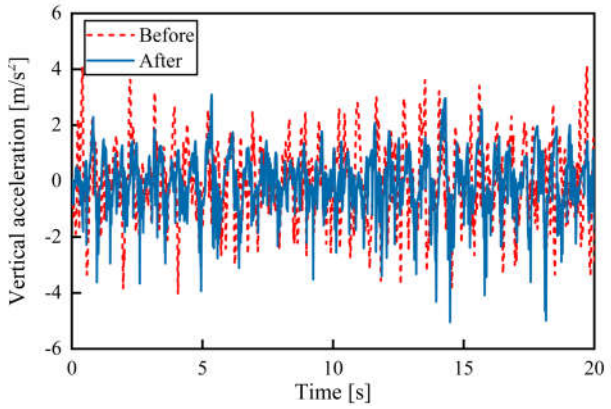

Fig. 12. Comparison of the vertical acceleration RMS value before and after optimization.

Fig. 13 shows the comparison of the suspension working space RMS value of the hydropneumatic suspension before and after optimization. The suspension working space RMS value of the hydropneumatic suspension before optimization was 7.868 mm. The suspension working space RMS value of the hydropneumatic suspension after optimization was 6.056 mm. Therefore, the suspension working space RMS value of the hydropneumatic suspension decreased by 23.0% using the APOA.

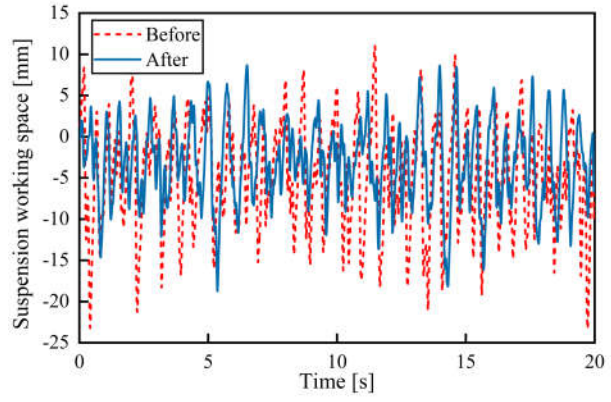

Fig. 13. Comparison of the suspension working space RMS value before and after optimization.

Fig. 14 shows the comparison of the dynamic tire load RMS value of the hydropneumatic suspension before and after optimization. The dynamic tire load RMS value of the hydropneumatic suspension before optimization was 4.839 kN. The dynamic tire load RMS value of the hydropneumatic suspension after optimization was 4.810 kN. Therefore, the dynamic tire load RMS value of the hydropneumatic suspension decreased by 0.62% using the APOA.

The analysis of the findings in Figs. 12–14 showed that the multiobjective APOA played an effective role in multiobjective optimization and the results were excellent.

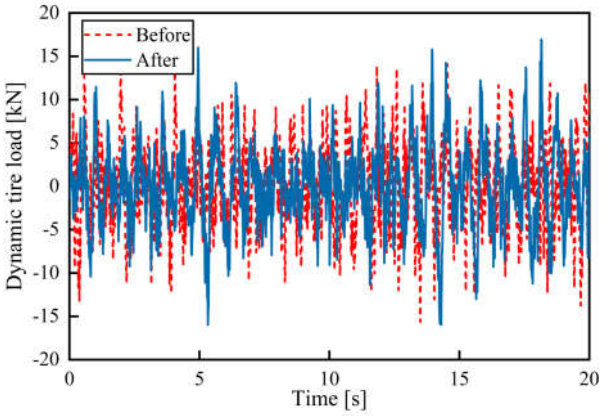

Fig. 14. Comparison of the dynamic tire load RMS value before and after optimization.

VI. Conclusion

This study investigated the performance and optimization of the hydropneumatic suspension of high-speed wheeled excavators. Based on the analyses, the following conclusions were drawn.

1. The spring force was controlled by the initial gas pressure, initial gas volume, and cross-sectional area of the piston. The spring force increased with the increase in the displacement.

2. The damping force was controlled by the cross-sectional area of the rod, cross-sectional area of the piston, opening area of orifices, and opening area of check valves.

3. The hydropneumatic suspension performed better compared with the leaf spring suspension. The vertical acceleration, suspension working space, and dynamic tire load of the hydropneumatic suspension decreased by 22.4%, 23.0%, and 0.62%, respectively, using the multiobjective APOA.

References

[1] B. Gong, X. Guo, S. Hu, and L. Xu, "Ride comfort optimization of a multi-axle heavy motorized wheel dump truck based on virtual and real prototype experiment integrated Kriging model," *Advances in Mechanical Engineering*, Vol. 7, No. 6, pp. 1-15, 2015.

[2] X. F. Yang, L. Yan, Y. J. Shen, H. C. Li and Y. L. Liu, "Dynamic per□formance analysis and parameters perturbation study of inerter-spring-damper suspension for heavy vehicle," *Journal of Low Frequency Noise, Vibration and Active Control*, Vol. 40, No. 3, pp. 1335-1350, 2020.

[3] X. L. Zhang, J. C. Liu, J. M. Nie, H. Wei and L. Chen, "Simulation analysis and experiment research on Hydro-Pneumatic ISD suspension," *Shock and Vibration*, Vol. 2021, pp. 1-14, 2021.

[4] G. V. Kinagi, S. P. Pitchuka and D. Sonawane, "Hydro-pneumatic suspension design for light military tracked vehicle," *SAE Technical Paper*, DOI: 10.4271/2012-01-1911, 2012.

[5] S. S. Han, Z. Q. Chao and X. B. Liu, "Research on the effects of hydro-pneumatic parameters on tracked vehicle ride safety based on cosimulation," *Shock and Vibration*, Vol. 2017, pp. 1256536-1-10, 2017.

[6] E. L. Zheng, S. Cui, T. Z. Yang, J. l. Xue, Y. Zhu and X. Z. Lin, "Simulation of the vibration characteristics for agricultural wheeled tractor with implement and front axle hydro-pneumatic suspension," *Shock and Vibration*, Vol. 2019, pp. 9135412-1-19, 2019.

[7] S. Wang, L. Zhen, X. H. Liu, Y. Cao and X. F. Li, "Active control of hydro-pneumatic suspension parameters of wheel loaders based on road condition identification," *International Journal of Advanced Robotic Systems*, Vol. 15, No. 6, pp. 1-13, 2018.

[8] X. F. Li, W. D. Lv, W. Zhang and H. Y. Zhao, "Research on dynamic behaviors of wheel loaders with different layout of hydro-pneumatic suspension," *Journal of Acceleration Vibroengineering*, Vol. 19, No. 7, pp. 5388-5404, 2018.

[9] Y.M. Yin, S. Rakheja, J.Yang and P. E. Boileau, "Characterization of a hydro-pneumatic suspension strut with gas-oil emulsion," *Mechanical Systems and Signal Processing*, Vol. 2018, No. 106, pp. 319-333, 2018.

[10] D. Z. Lin, F. Yang, D. Gong and S. Rakheja, "Design and experimental modeling of a compact hydro-pneumatic suspension strut," *Nonlinear Dynamics*, Vol. 100, No. 4, pp. 3307-3320, 2020.

[11] K. H. Kwon, M. Seo, H. S. Kim, T. H. Lee, J. Lee and S. Min, "Multi-objective optimisation of hydro-pneumatic suspension with gas-oil emulsion for heavy-duty vehicles," *Vehicle System Dynamics*, Vol. 58, No. 7, pp. 1146-1165, 2020.

[12] L. Yang, R. C. Wang, X. P. Meng, Z. Sun, W. Liu, and Y. Wang, "Performance analysis of a new hydropneumatic inerter□based suspension system with semi-active control effect," *Proceedings of the Institution of Mechanical Engineers-Part D: Journal of Automobile Engineering*, Vol. 234, No. 7, pp. 1883-1896, 2020.

[13] H. Pang, F. Liu and Z. Xu, "Variable universe fuzzy control for vehicle semi-active suspension system with MR damper combining fuzzy neural network and particle swarm optimization," *Neurocomputing*, Vol. 2018, No. 306, pp. 130-140, 2018.

[14] J. Zhao, P. K. Wong, Z. C. Xie, X. B. Ma, and C. Y. Wei, " Design of a road friendly SAS system for heavy-duty vehicles based on a fuzzy-hybrid-ADD and GH-control strategy," *Shock and Vibration*, Vol. 2016, pp. 1-7, 2016.

[15] N. M. Ghazaly and A. O. Moaaz, "Hydro-pneumatic passive suspension system performance analysis using amesim software," *International Journal of Vehicle Structures & Systems*, Vol. 12, No. 1, pp. 9-12, 2020.

[16] Z. H. Zhu, R. C. Wang, L. Yang, Z. Y. Sun and X. P. Meng, "Modelling and control of a semi-active dual-chamber hydro-pneumatic inerter-based suspension system." *Proceedings of the Institution of Mechanical Engineers, Part D: Journal of Automobile Engineering*, Vol. 235, No. 9, pp. 2355-2370, 2021.

[17] W. G. Wu, S. Zhang and Z. Y. Zhang, "Mathematical Simulations and On-Road Experimentations of the Vibration Energy Harvesting from Mining Dump Truck Hydro-Pneumatic Suspension," *Shock and Vibration*, Vol. 2019, pp. 1-16, 2019.

[18] H. Xu, Y. Zhao, C. Ye and F. Lin, "Integrated optimization for mechanical elastic wheel and suspension based on an improved artificial fish swarm algorithm," *Advances in Engineering Software*, Vol. 137, pp. 102722-1-8, 2019.

[19] L. P. Xie, J. C. Zeng and R. A. Formato, "Convergence analysis and performance of the extended artificial physics optimization algorithm," *Applied Mathematics and Computation*, Vol. 218, No. 8, pp. 4000-4011, 2011.

[20] K. Teeparthi and D. M. V. Kuma, "An improved artificial physics optimization algorithm approach for static power system security analysis," *Journal of The Institution of Engineers (India): Series B*, Vol. 101, No. 4, pp. 347-359, 2020.

[21] Y. Wang, J. C. Zeng and Y. Tan, "An artificial physics optimization algorithm for multi-objective problems based on virtual force sorting proceedings," *International Conference on Swarm, Evolutionary, and Memetic Computing*. Springer, Berlin, Heidelberg, 2010, pp. 615-622.

[22] C. Zhou, X. H. Liu, F. X. Xu and W. Chen, "Sliding mode switch control of adjustable hydro-pneumatic suspension based on parallel adaptive clonal selection algorithm," *Applied Sciences*, Vol. 10, No. 8, pp. 1-30, 2020.